

Three-Dimensional Magnetic Resonance Electrical Properties Tomography Based on Linear Integral Equation Derived from the Generalized Cauchy Formula

Motofumi Fushimi* and Takaaki Nara

Abstract—Magnetic resonance electrical properties tomography has attracted attentions as an imaging modality for reconstructing the electrical properties (EPs), namely conductivity and permittivity, of biological tissues. Current reconstruction algorithms assume that EPs are locally homogeneous, which results in the so-called tissue transition-region artifact. We previously proposed a reconstruction algorithm based on a Dbar equation that governed electric fields. The representation formula of its solution was given by the generalized Cauchy formula. Although this method gives an explicit reconstruction formula of EPs when two-dimensional approximation holds, an iterative procedure is required to deal with three-dimensional problems, and the convergence of this method is not guaranteed. In this paper, we extend our previous method to derive an explicit reconstruction formula of EPs that is effective even when the magnetic field and EPs vary along the body axis. The proposed method solves a linear system of equation derived from the generalized Cauchy formula using the conjugate gradient method with fast Fourier transform algorithm instead of directly performing a forward calculation, as was done in our previous method. Numerical simulations with cylinder and human-head models and phantom experiments show that the proposed method can reconstruct EPs precisely without iteration even in the three-dimensional case.

1. INTRODUCTION

Magnetic-resonance-based electrical properties tomography (EPT) is an emerging modality that noninvasively reconstructs the electrical properties (EPs), namely electric conductivity and dielectric permittivity, of biological tissues from the measured radiofrequency (RF) magnetic field obtained using a magnetic resonance imaging (MRI) scanner [1–4]. The retrieved EP maps reflect the physiological and pathological states of tissues and thus provide valuable information for clinical diagnoses. Several studies have shown that cancerous tissues have significantly different EP values compared with those of healthy tissues [5–7]. An increase in conductivity has been reported for hemorrhagic and ischemic stroke lesions [5]. Furthermore, conductivity maps can be used to calculate a patient-wise specific absorption rate (SAR) distribution [8], which is a safety criterion for preventing tissue heating in recent high-field MRI systems.

The electromagnetic fields transmitted by RF coils are governed by the following time-harmonic Maxwell's equations:

$$\nabla \times \mathbf{E}(\mathbf{r}) = -i\omega\mu_0\mathbf{H}(\mathbf{r}), \quad (1)$$

$$\nabla \times \mathbf{H}(\mathbf{r}) = i\omega \left(\epsilon_r(\mathbf{r})\epsilon_0 - i\frac{\sigma(\mathbf{r})}{\omega} \right) \mathbf{E}(\mathbf{r}) = i\omega\kappa(\mathbf{r})\mathbf{E}(\mathbf{r}), \quad (2)$$

Received 21 May 2020, Accepted 3 September 2020, Scheduled 17 September 2020

* Corresponding author: Motofumi Fushimi (motofumi-fushimi@g.ecc.u-tokyo.ac.jp).

The authors are with the Graduate School of Information Science and Technology, The University of Tokyo, Japan.

where $\mathbf{r} \in \Omega$ and Ω represents the body. Note that Ω does not include the electric source on an MRI coil. μ_0 and ϵ_0 are the magnetic permeability and the dielectric permittivity of free space, respectively, and $\omega/2\pi$ is the Larmor frequency of proton nuclei. We defined the complex permittivity, κ , as $\epsilon_r\epsilon_0 - i\sigma/\omega$. The magnetic permeability is assumed to be constant and identical to μ_0 throughout the entire body because the magnetic susceptibility of the human body is sufficiently small [9]. By using receiver coils, the positively rotating component of the magnetic field, $H^+ \equiv (H_x + iH_y)/2$, where the z -axis is set parallel to the body axis, can be measured inside Ω . Therefore, the EPT problem is to reconstruct κ inside the region of interest (ROI) denoted by $D \subset \Omega$ from the measured H^+ data.

A simple approach for the EPT inverse problem is to derive Helmholtz's equation for H^+ by neglecting the spatial variation of κ [10,11]. Although this approach realizes a simple pointwise reconstruction of κ , unstable results are obtained because this method requires second-order derivatives of the measured magnetic field data, which amplify the high-frequency measurement noise. Some stabilized versions of this method have been proposed [12,13]. However, a limitation of this method is that serious errors occur at tissue transition-regions where EPs vary [14,15].

Methods for removing the artifact at the tissue transition-region artifacts can be generally divided into two types. The first approach is based on local relations represented by partial differential equations (PDEs). Song et al. [16] and Ammari et al. [17] proposed iterative methods that solve the nonlinear PDE for κ expressed by the measured H^+ data for cases where EPs are two- and three-dimensionally distributed, respectively. Hafalir et al. proposed the cr-MREPT method [18]. They introduced the inverse of admittivity, $\lambda \equiv 1/i\omega\kappa$, and derived a linear PDE for λ . They solved the linear PDE using the finite element method (FEM). The main disadvantage of these PDE-based local methods is that the Laplacian of the measured data must be calculated, which amplifies noise. Some authors proposed solving a system of equations for both κ and $\nabla\kappa$ by utilizing multiple sets of magnetic field data obtained using a multichannel coil [19–24]. Here, we assume quadrature birdcage coil (QBC) configurations, which are in common use.

The second approach is based on global relations represented by integral equations (IEs). Balidemaj et al. proposed the CSI-EPT method [25], which is based on the scattering problem formulation. The IE is solved using an optimization procedure called the contrast source inversion method. However, as pointed out by Arduino et al. [26], the IE representation includes Green's function, which is associated with the governing PDE and specific boundary conditions. The explicit representation of this Green's function can be obtained only when the specific simple boundary conditions or radiation conditions are given. Thus, to deal with the more complicated case of using an RF shield, which is mathematically modeled as a perfect electric conductor shield, one must calculate Green's function numerically by solving a FEM problem at each iteration.

We previously proposed a Dbar-equation-based reconstruction method [27,28]. In this method, with the two-dimensional (2D) plane approximation, $H_z = 0$ and $\partial_z H^+ = 0$, the following complex form of Maxwell's equations were derived:

$$\bar{\partial}E_z(\zeta) = \omega\mu_0H^+(\zeta), \quad (3)$$

$$4\partial H^+(\zeta) = -\omega\kappa(\zeta)E_z(\zeta). \quad (4)$$

where $\zeta = x + iy$, $\zeta \in D$ and D is the 2D ROI. We defined complex differential operators, ∂ and $\bar{\partial}$, as follows:

$$\partial \equiv \frac{1}{2}(\partial_x - i\partial_y), \quad (5)$$

$$\bar{\partial} \equiv \frac{1}{2}(\partial_x + i\partial_y). \quad (6)$$

In this method, we split the whole reconstruction procedure of calculating κ from H^+ into two parts: the E_z reconstruction part and the κ reconstruction part. In the first part, we solve Eq. (3) for E_z . This type of PDE is known as the Dbar equation. The explicit representation of the solution is given by the generalized Cauchy formula [29]. Once we obtain E_z , κ is directly reconstructed as the ratio of ∂H^+ to E_z from Ampere's law given in Eq. (4). Because this method does not need to calculate the second derivative of H^+ , it is more robust against noise. This representation formula holds for an ROI, D , with any boundary shape.

However, this method is restricted to the 2D case when κ is homogeneous in the axial direction. Therefore, in this paper, we extend our previous method and propose a reconstruction method that can be applied to the general three-dimensional problem.

2. THEORY

2.1. Governing Equation of Electric Field

In this section, we derive the governing equation of E_z that accounts for the variation of EPs along the axial direction. By taking the $(x + iy)$ -component of Eq. (1), it follows that

$$\bar{\partial}E_z = \omega\mu_0H^+ + \partial_zE^+, \tag{7}$$

where $E^+ \equiv (E_x + iE_y)/2$. In our previous method, we neglected the E^+ term in Eq. (7), resulting in Eq. (3). By taking the $(x + iy)$ -component of Eq. (2), it follows that E^+ is related to the z -derivative of H^+ and κ as follows:

$$E^+ = \frac{\partial_zH^+}{\omega\kappa} \tag{8}$$

Therefore, neglecting E^+ is equivalent to assuming $\partial_zH^+ = 0$. By substituting Eq. (8) into Eq. (7), we get

$$\bar{\partial}E_z = \omega\mu_0H^+ + \partial_z\left(\frac{\partial_zH^+}{\omega\kappa}\right). \tag{9}$$

To properly evaluate E^+ and derive a PDE of E_z in terms of the measured H^+ and its derivatives including ∂_zH^+ , we first eliminate κ in Eq. (9). Eq. (4) says that the EPs are calculated as the ratio of the magnetic field gradient to the electric field as follows:

$$\frac{1}{\kappa} = -\frac{\omega E_z}{4\partial H^+}, \tag{10}$$

when $\partial H^+ \neq 0$ holds. Substituting Eq. (10) into Eq. (9) yields

$$\bar{\partial}E_z = \omega\mu_0H^+ - \partial_z\left(\frac{\partial_zH^+}{4\partial H^+}E_z\right). \tag{11}$$

This is a complex PDE for E_z that accounts for the effect of ∂_zH^+ . If ∂_zH^+ is assumed to be zero, Eq. (11) reduces to Eq. (3) used in our previous method.

To deal with the case when $\partial H^+ \simeq 0$, we estimate $1/\kappa$ by minimizing the following cost functional:

$$J\left(\frac{1}{\kappa}\right) = \left|\frac{\omega}{4}E_z + \partial H^+\frac{1}{\kappa}\right|^2 + \alpha^2\left|\frac{1}{\kappa}\right|^2. \tag{12}$$

This corresponds to estimating $1/\kappa$ with Tikhonov regularization. The estimate can be calculated in a pointwise manner as follows:

$$\frac{1}{\kappa} = -\frac{\omega}{4}\frac{\overline{\partial H^+}}{|\partial H^+|^2 + \alpha^2}E_z, \tag{13}$$

where $\alpha > 0$ is a regularization parameter. Substituting Eq. (13) into Eq. (7) and (8) yields

$$\bar{\partial}E_z = \omega\mu_0H^+ - \partial_z\left(\frac{\partial_zH^+}{4}\frac{\overline{\partial H^+}}{|\partial H^+|^2 + \alpha^2}E_z\right). \tag{14}$$

Eq. (14) is our fundamental equation that describes E_z in terms of the measured H^+ and its derivatives.

2.2. Linear Integral Equation for E_z and Its Solution

In this section, we derive a linear integral equation for E_z from Eq. (14). Given a simply connected 2D domain D bounded by a simple closed contour $C \equiv \partial D$ and a function $f \in C(\bar{D}) \cap C^1(D)$ with $\bar{\partial}f = g$, the following formula holds [29]:

$$f(\zeta) = \frac{1}{2\pi i} \int_C \frac{f(\zeta')}{\zeta' - \zeta} d\zeta' - \frac{1}{\pi} \iint_D \frac{g(\zeta')}{\zeta' - \zeta} dx' dy', \quad (15)$$

where $\zeta = x + iy$ and $\zeta' = x' + iy'$. Eq. (15) is called the generalized Cauchy formula and gives an explicit representation of the solution of a Dbar equation, $\bar{\partial}f = g$. Substituting Eqs. (4) and (14) into Eq. (15) leads to

$$E_z(\zeta) = \frac{1}{2\pi i} \int_C \frac{-4\partial H^+ / (\omega\kappa)}{\zeta' - \zeta} d\zeta' - \frac{1}{\pi} \iint_D \frac{\omega\mu_0 H^+ - \partial_z(AE_z)}{\zeta' - \zeta} dx' dy', \quad (16)$$

where, for simplicity, we define A as follows:

$$A \equiv \frac{\partial_z H^+}{4} \frac{\overline{\partial H^+}}{|\partial H^+|^2 + \alpha^2}. \quad (17)$$

Eq. (16) includes E_z in its integral term and thus is an integral equation for E_z . By defining an operator, T , as

$$T[f](\zeta) \equiv -\frac{1}{\pi} \iint_D \frac{f}{\zeta' - \zeta} dx' dy', \quad (18)$$

and $L[f]$ as $-T[\partial_z(Af)]$, Eq. (16) can be rewritten as follows:

$$(I - L)[E_z] = E_z^0, \quad (19)$$

where I is the identity operator and

$$E_z^0 \equiv \frac{1}{2\pi i} \int_C \frac{-4\partial H^+ / (\omega\kappa)}{\zeta' - \zeta} d\zeta' - \frac{1}{\pi} \iint_D \frac{\omega\mu_0 H^+}{\zeta' - \zeta} dx' dy'. \quad (20)$$

This linear integral equation can be solved using the conjugate gradient (CG) method. In the CG method, the forward operation must be calculated for each iteration. In our case, the operator T is defined as a convolution and thus can be efficiently calculated using the fast Fourier transform (FFT). Note that the convolution is done in a finite domain, D , instead of the whole complex plane. Therefore some modification of the convolution kernel is needed to properly calculate the integration via FFT. The details are described in Appendix A.

Once we obtain the estimation of E_z , κ is directly calculated as the ratio of ∂H^+ to E_z according to Eq. (4).

2.3. Comparison with Iterative Correction Method

In this section, we compare the proposed method with our previous method that uses the 2D assumption to obtain the initial estimate, which is given by E_z^0 in Eq. (20), and iteratively correct the effect of $\partial_z H^+$.

With the current estimate of the electric field, $E_z^{(n)}$, the updated estimate, $E_z^{(n+1)}$ is obtained by substituting $E_z^{(n)}$ into the right hand side of Eq. (16) and performing the forward integral calculation. By using the operator, L , this update procedure can be written as follows:

$$E_z^{(n+1)} = E_z^0 + L[E_z^{(n)}]. \quad (21)$$

Eq. (19) can be rewritten as follows using the Neumann expansion of L :

$$E_z = E_z^0 + L[E_z^0] + L[L[E_z^0]] + \dots \quad (22)$$

A comparison of Eq. (22) with Eq. (21) indicates that the n -th estimate of the iteration method corresponds to the solution of Eq. (16) when $(I - L)^{-1}[E_z^0]$ is approximated as the first n terms of Eq. (22).

Note that the Neumann expansion of $(I - L)^{-1}$ is valid only when $\|L\| < 1$ holds, where $\|L\|$ represents the operator norm of L . In our case, $L[f] = -T[\partial_z(Af)]$ with A given by Eq. (17). Therefore, the norm of L depends on $\partial_z H^+$ and ∂H^+ . It is known that when the birdcage coil typically used in modern MR scanners is driven in quadrature mode, ∂H^+ gets very small around the center of the human body. Thus, if we include the center of the body in the ROI, $\|L\| < 1$ does not hold, resulting in a non-converged case of the iteration method. Our proposed method, in contrast, is free from such non-convergent results because it does not use the Neumann expansion.

3. METHODS

3.1. Numerical Simulations

A 16-leg high-pass shielded birdcage coil with a diameter of 240 mm and a height of 270 mm was constructed. A cylindrical phantom with a diameter of 144 mm and a height of 270 mm was loaded into the birdcage coil. The optimal capacitance value of the birdcage coil was determined according to the method proposed by Gurler et al. [30]. The magnetic field was excited at 123.2 MHz (corresponding to a 2.89 T MRI system) in quadrature excitation mode, in which the coil was driven by two ports 90° apart from each other and with a 90° phase difference. H^+ was obtained on a $180 \text{ mm} \times 180 \text{ mm}$ square region centered at the origin in the central slice ($z = 0$) with a matrix size of 128×128 (a resolution of about $1.4 \text{ mm} \times 1.4 \text{ mm}$). Two models (model 1 in Fig. 1(a), which we call the Shepp-Logan model, and model 2 in Fig. 1(b), which we call the human brain model) were constructed as loading objects. True EP maps of each model in the ROI are shown in Fig. 2.

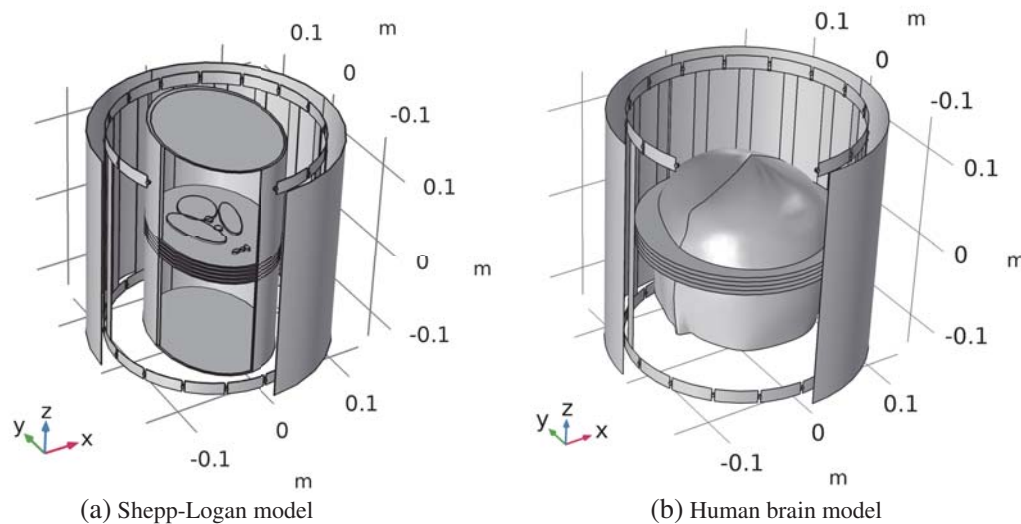


Figure 1. Simulation setups for (a) Shepp-Logan model and (b) human brain model.

The computation of H^+ was performed using the FEM software, COMSOL Multiphysics 5.3 (COMSOL Inc.). MATLAB R2019a (The MathWorks Inc.) was used for all reconstruction processes.

3.2. Phantom Experiments

A phantom composed of two cylindrical regions (inner and outer regions) was used. The conductivity of the phantom was modified by adding NaCl. The permittivity was constant and identical to that of water. We added 6 and 2 g/l of NaCl in regions 1 and 2, respectively. The conductivities of the inner and outer regions were 0.94 and 0.43 S/m, as measured using a conductivity meter (Hanna Instruments, HI 8733). We used CuSO_4 (1.5 g/l) to adjust the T_1 value of the phantom.

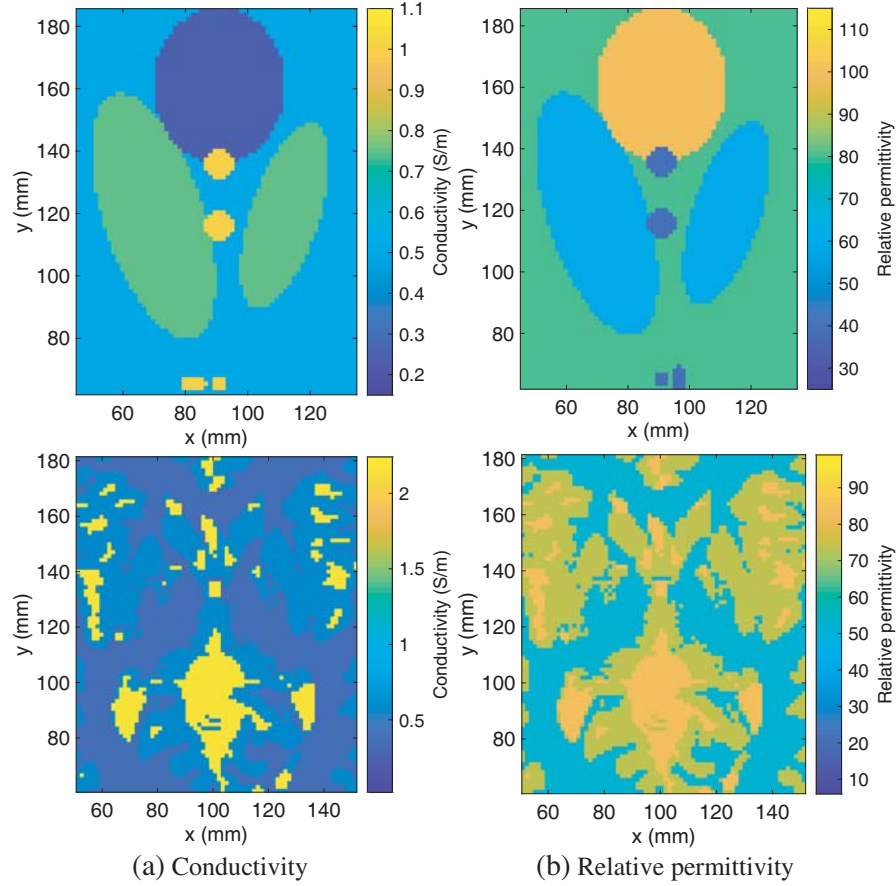


Figure 2. True EP maps of two simulation models: Shepp-Logan model (top) and human brain model (bottom). (a) Conductivity and (b) relative permittivity.

The magnitude of H^+ can be measured using the B1 mapping technique. We used the double angle method proposed in [31]. In this method, $|H^+|$ is calculated from two gradient echo images with 60° and 120° flip angles, respectively, as follows:

$$|H^+| = \frac{\cos^{-1}(|S_{\text{GRE},120}|/2|S_{\text{GRE},60}|)}{\mu_0\gamma\tau}, \quad (23)$$

where γ is the gyromagnetic ratio, and τ is the duration time of the RF pulse. The phase of H^+ is calculated from two spin echo images with opposite readout directions as follows:

$$\angle H^+ = \frac{(\angle S_{\text{SE,AP}} + \angle S_{\text{SE,PA}})/2}{2}. \quad (24)$$

Note that we used the transceive phase approximation [32] to separate transmit phase $\angle H^+$ from receive phase $\angle H^-$.

The experiment was conducted using the 3 T MR scanner Magnetom Prisma (Siemens) at the University of Tokyo.

4. RESULTS

4.1. Simulation Results

Figure 3 shows the reconstruction results for the Shepp-Logan model when 1% Gaussian noise was added. As shown in Fig. 3(a), in the previous method with no iteration, both conductivity and relative

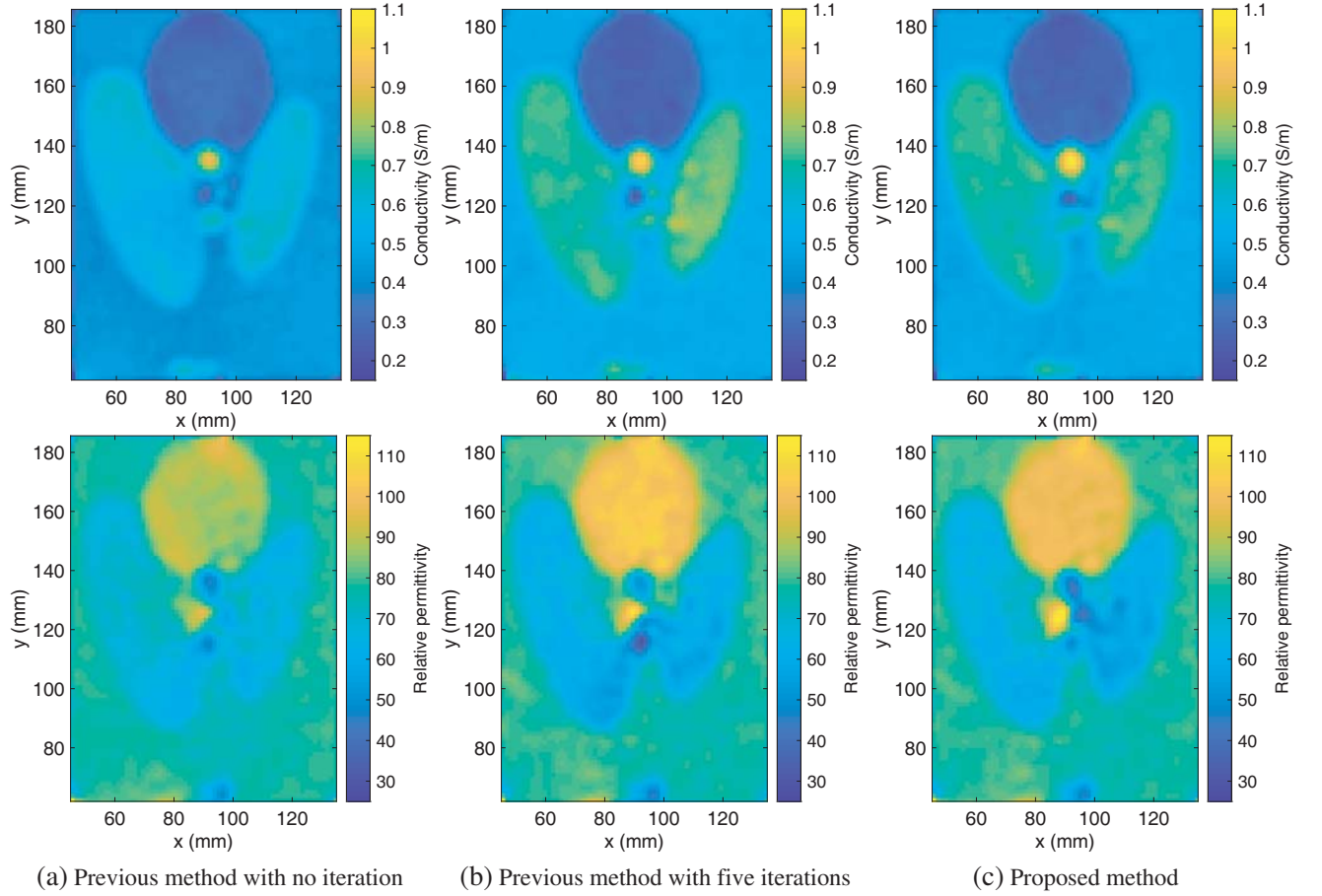


Figure 3. Reconstruction results of conductivity (top) and relative permittivity (bottom) for Shepp-Logan model for a signal-to-noise ration of 40 dB. (a) Previous method with no iteration, (b) previous method with five iterations, and (c) proposed method.

permittivity have lower values than those in the true maps. This is because the z derivative of the magnetic field is ignored in the previous method with no iteration. The effect of $\partial_z H^+$ is properly corrected for in the previous method after five iterations, as shown in Fig. 3(b). The proposed method also accurately estimated the conductivity and relative permittivity maps without iteration, as shown in Fig. 3(c).

Figure 4 shows relative errors after each iteration measured using the L2 norm expressed as

$$\sqrt{\frac{1}{N} \sum_{i=1}^N \frac{|\kappa(\zeta_i) - \kappa_{\text{true}}(\zeta_i)|}{|\kappa_{\text{true}}(\zeta_i)|}}, \quad (25)$$

where i is the index of points in the ROI, and N is the number of pixels in the ROI. As shown in Fig. 4, both conductivity and relative permittivity converged after a single iteration. The relative errors of the proposed method have lower values than those of the previous method after five iterations.

Figure 5 plots the reconstruction results on the line $x = 0$. The values for the proposed method (red line) are closer to the true values (black line) than are those for the previous method (blue line).

Figure 6 shows the reconstruction results for the human brain model when no noise was added. As shown in Fig. 6(a), both conductivity and relative permittivity have lower values than those in the true maps. This brain model has EPs varying along the z -axis and thus the effect of $\partial_z H^+$ is more prominent here than in the Shepp-Logan model. The results of the previous method after five iterations have serious errors as shown in Fig. 6(b). This is because the zero-point artifact is severe in

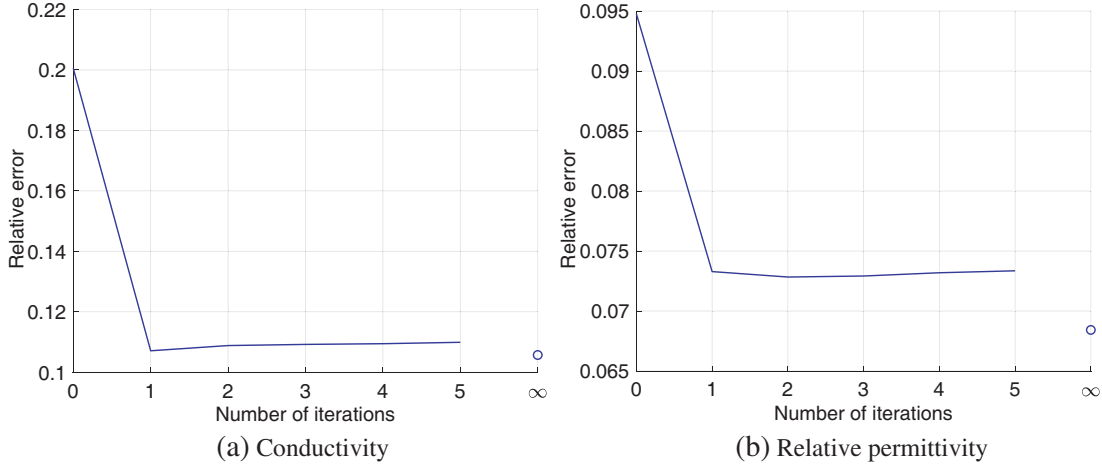


Figure 4. Relative errors of (a) conductivity and (b) relative permittivity at each iteration of the previous method and for the proposed method. ∞ on the horizontal axis indicates the result for the proposed method.

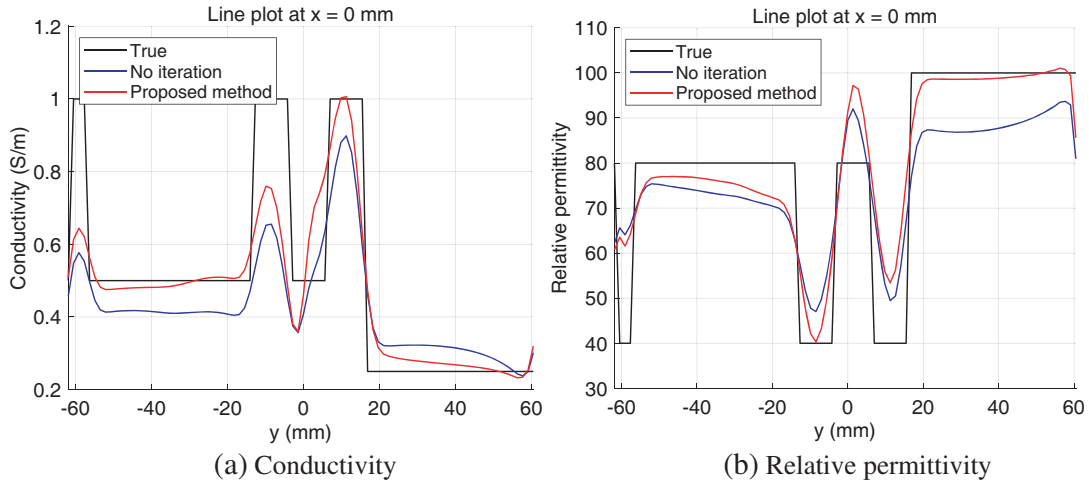


Figure 5. Line plot at $y = 0$ mm when no noise was added.

this model and convergence is not guaranteed in this case. The proposed method correctly incorporates the effect of $\partial_z H^+$ and gives relatively stable results, as shown in Fig. 6(c). This is confirmed in Fig. 7. The relative errors of the previous method do not decrease with increasing number of iterations. The proposed method yields the lowest errors in both conductivity and relative permittivity results.

The difference between the results of the two models is explained below. For the Shepp-Logan model, the iterative correction properly worked and only a single iteration was needed to obtain converged results. This is because the zero-point artifact is not severe in the Shepp-Logan model and thus the condition $\|L\| < 1$ may be satisfied when sufficient regularization is applied to calculate the inverse of ∂H^+ . For the human brain model, in contrast, the iteration did not converge. This is because the zero-point artifact is severe in this model and the condition $\|L\| < 1$ may not be satisfied even when the inversion of ∂H^+ is regularized.

4.2. Experimental Results

Figure 8 shows the reconstructed conductivities of the experimental phantom. The result of the standard EPT method is also shown in Fig. 8(a) because standard EPT is free from 2D approximation and,

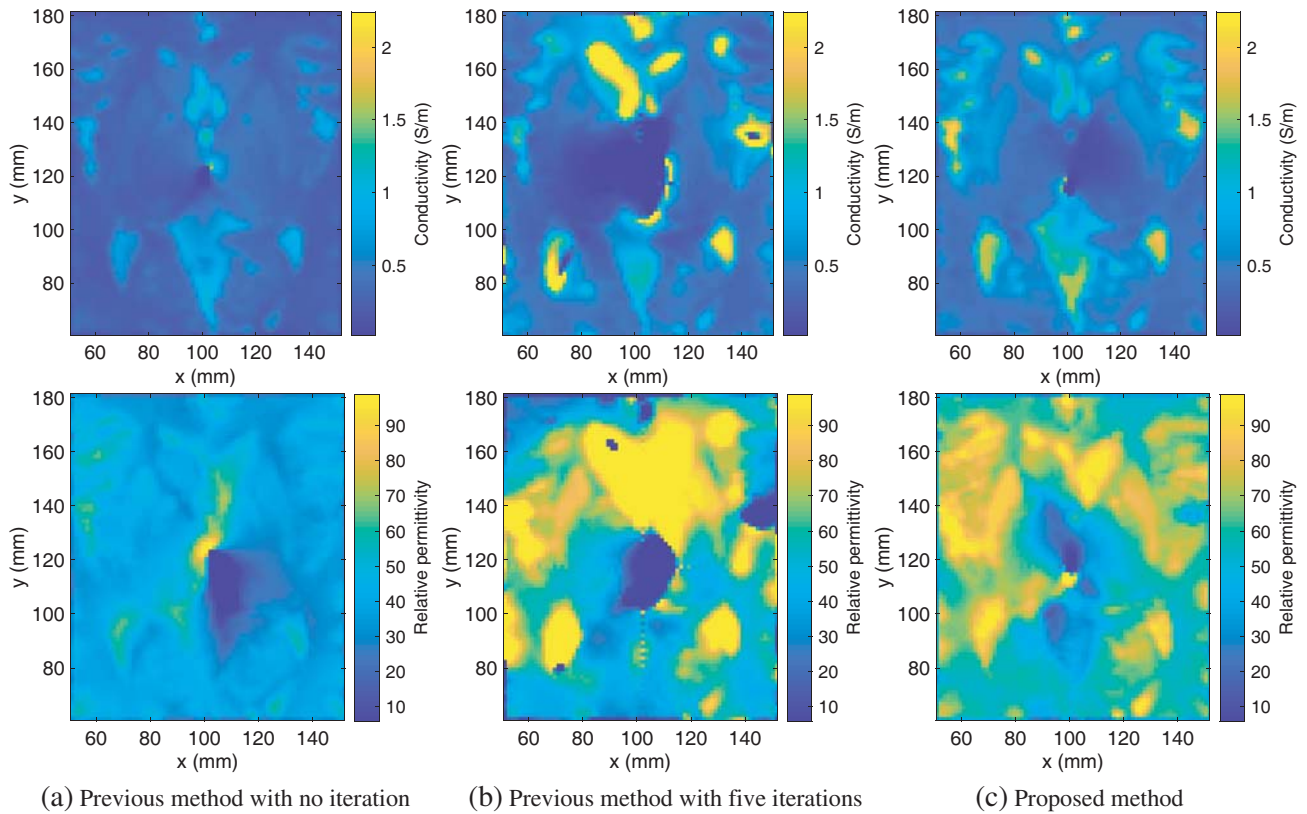


Figure 6. Reconstruction results of conductivity (top) and relative permittivity (bottom) for human brain model for a signal-to-noise ration of 40 dB. (a) Previous method with no iteration, (b) previous method with five iterations, and (c) proposed method.

with sufficient smoothing filtering, it yields accurate results except at tissue-transition regions. The conductivity values obtained using the previous method are lower than those of the standard method, whereas those of the proposed method are very close in both the inner and outer cylindrical regions. These values also match those measured using an electric probe.

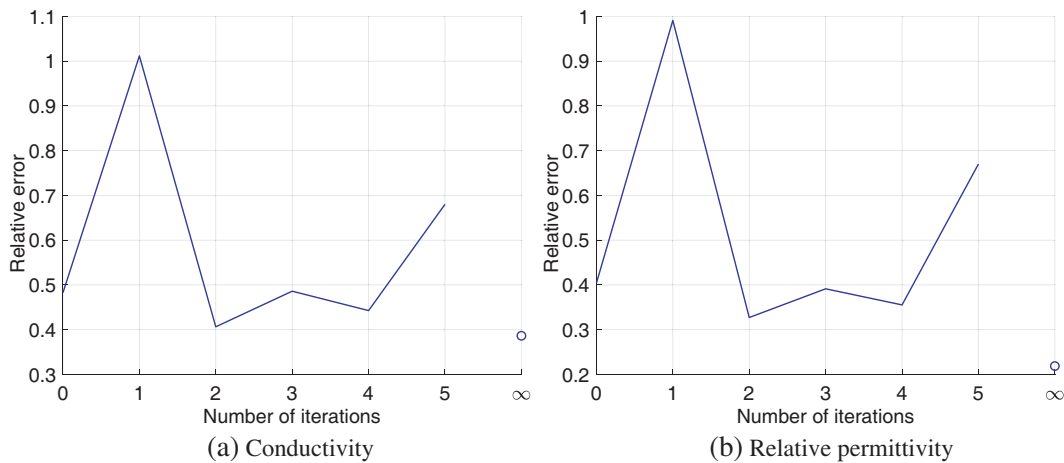


Figure 7. Relative errors at each iteration of the previous method and for the proposed method.

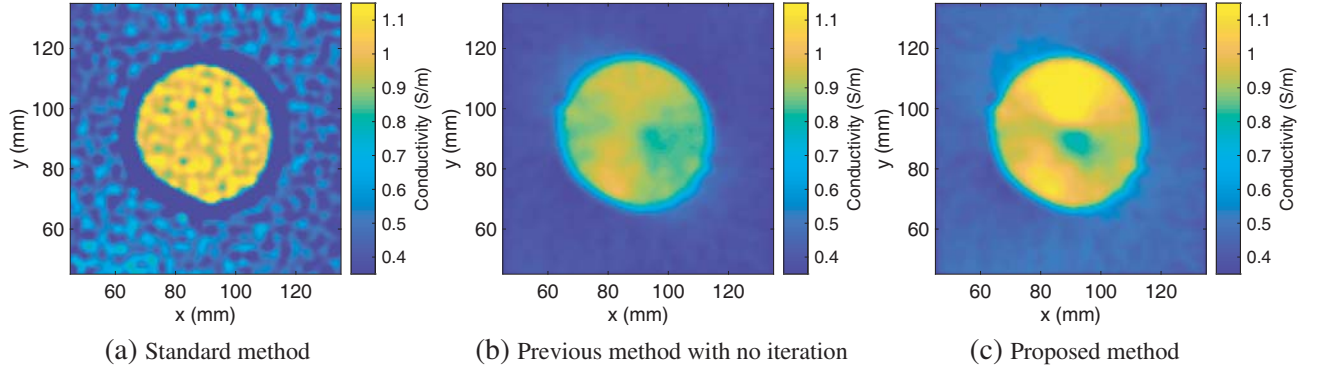


Figure 8. Reconstruction results of conductivity (top) and relative permittivity (bottom) for the phantom experiment. (a) Standard method, (b) previous method with no iteration, and (c) proposed method.

5. CONCLUSION

In this paper, we extended our previous method to derive an explicit reconstruction formula of EPs that is effective even when the magnetic field and EPs vary along the body axis. The proposed method solves a linear integral equation derived from the generalized Cauchy formula using the CG method with the FFT algorithm instead of directly performing a forward calculation as was done in our previous method. Numerical simulations with cylinder and human-head models and phantom experiments show that the proposed method can reconstruct EPs precisely without iteration even in the three-dimensional case.

ACKNOWLEDGMENT

This work was partly supported by JSPS KAKENHI Grant Number 19H04438.

APPENDIX A. DERIVATION OF CAUCHY KERNEL FOR A FINITE-DOMAIN INTEGRAL

By extending the integrand f with zero-padding, the operation $T[f]$ can be regarded as a convolution of f with the Cauchy kernel as follows:

$$T[f](\zeta) = \frac{1}{\pi} \iint_{\mathbb{R}^2} \frac{\tilde{f}(\zeta')}{\zeta - \zeta'} dx' dy' = \tilde{f}(\zeta) * \frac{1}{\pi\zeta}, \quad (\text{A1})$$

where

$$\tilde{f}(\zeta) = \begin{cases} f(\zeta) & \zeta \in D, \\ 0 & \zeta \in \mathbb{R}^2 \setminus \overline{D} \end{cases} \quad (\text{A2})$$

To realize this convolution as a pointwise product in the Fourier domain, we derive the Fourier-domain representation of $G(x, y) = 1/(\pi(x + iy))$. Given that $G(x, y)$ is a fundamental solution of the Dbar equation, it holds that

$$\frac{1}{2}(\partial_x + i\partial_y)G(x, y) = \delta(x)\delta(y). \quad (\text{A3})$$

Applying the Fourier transform to both sides of Eq. (A3) yields

$$\mathcal{F}[G] = \frac{1}{\pi i} \frac{1}{u + iv}. \quad (\text{A4})$$

Note that this function is singular at the origin. Following to Vico [33], we modify the function to derive a non-singular version without any approximation.

Because \tilde{f} has a finite support, D , by its definition and thus the range that the convolution has nonzero value is bounded, it holds that

$$I(\zeta) = \tilde{f}(\zeta) * \frac{\chi_R(\zeta)}{\pi\zeta} \quad (\text{A5})$$

without any approximation, where χ_R is the characteristic function of the region R . R can be taken as a circle with radius a , where a is determined according to D . In this case, $\chi_R = U(a - r)$ holds, where U is the step function and $r = \sqrt{x^2 + y^2}$. Then, the Dbar derivative of $\chi_R G$ can be calculated as follows:

$$\begin{aligned} \frac{1}{2}(\partial_x + i\partial_y)(\chi_R(x, y)G(x, y)) &= U(a - r)\delta(x)\delta(y) - \frac{\exp(i\theta)\delta(r - a)}{2} \frac{1}{\pi\zeta} \\ &= \delta(x)\delta(y) - \frac{\delta(r - a)}{2\pi r}, \end{aligned} \quad (\text{A6})$$

where $\theta = \tan^{-1}(y/x)$. Compared to Eq. (A3), Eq. (A6) has an additional term, namely the delta function at $r = a$, reflecting the effect of $U(a - r)$. The Fourier spectrum of the second term on the right-hand side is given as follows:

$$\begin{aligned} \mathcal{F}\left[-\frac{\delta(r - a)}{2\pi r}\right] &= -\frac{1}{2\pi} \iint_{\mathbb{R}^2} \frac{\delta(r - a)}{r} \exp(-2\pi i(ux + vy)) dx dy \\ &= -J_0(2\pi a\rho), \end{aligned} \quad (\text{A7})$$

where $\rho = \sqrt{u^2 + v^2}$ and J_0 is the zeroth-order Bessel function of the first kind. By applying the Fourier transform to Eq. (A6) and substituting Eq. (A7), it holds that

$$\mathcal{F}\left[\frac{\chi_R(x, y)}{\pi(x + iy)}\right] = \frac{1}{\pi i} \frac{1 - J_0(2\pi a\rho)}{u + iv}. \quad (\text{A8})$$

This function can be used to calculate the convolution with the Cauchy kernel in a finite domain and is not singular at the origin.

REFERENCES

1. Katscher, U., D.-H. Kim, and J. K. Seo, "Recent progress and future challenges in MR electric properties tomography," *Comput. Math. Methods Med.*, Vol. 2013, 1–11, 2013.
2. Zhang, X., J. Liu, and B. He, "Magnetic-resonance-based electrical properties tomography: A review," *IEEE Rev. Biomed. Eng.*, Vol. 7, 87–96, 2014.
3. Katscher, U. and C. A. T. van den Berg, "Electric properties tomography: Biochemical, physical and technical background, evaluation and clinical applications," *NMR Biomed.*, Vol. 30, No. 8, 1–15, 2017.
4. Liu, J., Y. Wang, U. Katscher, and B. He, "Electrical properties tomography based on B1 maps in MRI: Principles, applications, and challenges," *IEEE Trans. Biomed. Eng.*, Vol. 64, No. 11, 2515–2530, 2017.
5. Joines, W. T., Y. Zhang, C. Li, and R. L. Jirtle, "The measured electrical properties of normal and malignant human tissues from 50 to 900 MHz," *Med. Phys.*, Vol. 21, No. 4, 547–550, 1994.
6. Lazebnik, M., D. Popovic, L. McCartney, C. B. Watkins, M. J. Lindstrom, J. Harter, S. Sewall, T. Ogilvie, A. Magliocco, T. M. Breslin, W. Temple, D. Mew, J. H. Booske, M. Okoniewski, and S. C. Hagness, "A large-scale study of the ultrawideband microwave dielectric properties of normal, benign and malignant breast tissues obtained from cancer surgeries," *Phys. Med. Biol.*, Vol. 52, No. 20, 6093–6115, 2007.
7. Li, Z., W. Wang, Z. Cai, S. Han, S. Lin, L. He, M. Chen, D. Pan, G. Deng, S. Duan, and S. X. Xin, "Variation in the dielectric properties of freshly excised colorectal cancerous tissues at different tumor stages," *Bioelectromagnetics*, Vol. 38, No. 7, 522–532, 2017.

8. Collins, C. M., W. Liu, J. Wang, R. Gruetter, J. T. Vaughan, K. Ugurbil, and M. B. Smith, "Temperature and SAR calculations for a human head within volume and surface coils at 64 and 300 MHz," *J. Magn. Reson.*, Vol. 19, No. 5, 650–656, 2004.
9. Schenck, J. F., "The role of magnetic susceptibility in magnetic resonance imaging: MRI magnetic compatibility of the first and second kinds," *Med. Phys.*, Vol. 23, No. 6, 815–850, 1996.
10. Haacke, E. M., L. S. Petropoulos, E. W. Nilges, and D. H. Wu, "Extraction of conductivity and permittivity using magnetic resonance imaging," *Phys. Med. Biol.*, Vol. 36, No. 6, 723–734, 1991.
11. Wen, H., "Noninvasive quantitative mapping of conductivity and dielectric distributions using RF wave propagation effects in high-field MRI," *Proc. SPIE Med. Imag.*, Vol. 5030, 471–477, San Diego, CA, USA, 2003.
12. Katscher, U., T. Voigt, C. Findekle, P. Vernickel, K. Nehrke, and O. Dössel, "Determination of electric conductivity and local SAR via B1 mapping," *IEEE Trans. Med. Imag.*, Vol. 28, No. 9, 1365–1374, 2009.
13. Voigt, T., U. Katscher, and O. Doessel, "Quantitative conductivity and permittivity imaging of the human brain using electric properties tomography," *Magn. Reson. Med.*, Vol. 66, No. 2, 456–466, 2011.
14. Seo, J. K., M.-O. Kim, J. Lee, N. Choi, E. J. Woo, H. J. Kim, O. I. Kwon, and D.-H. Kim, "Error analysis of nonconstant admittivity for MR-based electric property imaging," *IEEE Trans. Med. Imag.*, Vol. 31, No. 2, 430–437, 2012.
15. Duan, S., C. Xu, G. Deng, J. Wang, F. Liu, and S. X. Xin, "Quantitative analysis of the reconstruction errors of the currently popular algorithm of magnetic resonance electrical property tomography at the interfaces of adjacent tissues," *NMR Biomed.*, Vol. 29, No. 6, 744–750, 2016.
16. Song, Y. and J. K. Seo, "Conductivity and permittivity image reconstruction at the Larmor frequency using MRI," *SIAM J. Appl. Math.*, Vol. 73, No. 6, 2262–2280, 2013.
17. Ammari, H., H. Kwon, Y. Lee, K. Kang, and J. K. Seo, "Magnetic-resonance-based reconstruction method of conductivity and permittivity distribution at Larmor frequency," *Inverse Problems*, Vol. 31, No. 10, 105001, 2015.
18. Hafalir, F. S., O. F. Oran, N. Gurler, and Y. Z. Ider, "Convection-reaction equation based magnetic resonance electrical properties tomography (cr-MREPT)," *IEEE Trans. Med. Imag.*, Vol. 33, No. 3, 777–793, 2014.
19. Sodickson, D. K., L. Alon, C. M. Deniz, R. Brown, B. Zhang, G. C. Wiggins, G. Y. Cho, N. B. Eliezer, D. S. Novikov, R. Lattanzi, Q. Duan, L. A. Sodickson, and Y. Zhu, "Local Maxwell tomography using transmit-receive coil arrays for contact-free mapping of tissue electrical properties and determination of absolute RF phase," *Proc. ISMRM 20th Annual Meeting*, 387, Melbourne, VIC, Australia, 2012.
20. Sodickson, D. K., L. Alon, C. M. Deniz, N. B. Eliezer, L. A. Sodickson, C. M. Collins, G. C. Wiggins, and D. S. Novikov, "Generalized local Maxwell tomography for mapping of electrical property gradients and tensors," *Proc. ISMRM 21st Annual Meeting*, 4175, Salt Lake City, UT, USA, 2013.
21. Liu, J., X. Zhang, P.-F. V. de Moortele, S. Schmitter, and B. He, "Determining electrical properties based on B1 fields measured in an MR scanner using a multi-channel transmit/receive coil: A general approach," *Phys. Med. Biol.*, Vol. 58, No. 7, 4395–4408, 2013.
22. Zhang, X., S. Schmitter, P.-F. V. de Moortele, J. Liu, and B. He, "From complex B₁ mapping and to local SAR estimation for human brain MR imaging using multi-channel transceiver coil at 7 T," *IEEE Trans. Med. Imag.*, Vol. 32, No. 6, 1058–1067, 2013.
23. Liu, J., X. Zhang, S. Schmitter, P.-F. V. de Moortele, and B. He, "Gradient-based electrical properties tomography (gEPT): A robust method for mapping electrical properties of biological tissues in vivo using magnetic resonance imaging," *Magn. Reson. Med.*, Vol. 74, No. 3, 634–646, 2015.
24. Liu, J., P.-F. V. de Moortele, X. Zhang, Y. Wang, and B. He, "Simultaneous quantitative imaging of electrical properties and proton density from B₁ maps using MRI," *IEEE Trans. Med. Imag.*, Vol. 35, No. 9, 2064–2073, 2016.

25. Balidemaj, E., C. A. van den Berg, J. Trinks, A. L. van Lier, A. J. Nederveen, L. J. A. Stalpers, H. Crezee, and R. F. Remis, "CSI-EPT: A contrast source inversion approach for improved MRI based electric properties tomography," *IEEE Trans. Med. Imag.*, Vol. 34, No. 9, 1788–1796, 2015.
26. Arduino, A., L. Zilberti, M. Chiampi, and O. Bottauscio, "CSI-EPT in presence of RF-shield for MR-coils," *IEEE Trans. Med. Imag.*, Vol. 36, No. 7, 1396–1404, 2017.
27. Nara, T., T. Furuichi, and M. Fushimi, "An explicit reconstruction method for magnetic resonance electrical property tomography base on the generalized Cauchy formula," *Inverse Problems*, Vol. 33, No. 10, 105005, 2017.
28. Fushimi, M. and T. Nara, "A boundary-value-free reconstruction method for magnetic resonance electrical properties tomography based on the neumann-type integral formula over a circular region," *SICE JCMSI*, Vol. 10, No. 6, 571–578, 2017.
29. Ablowitz, M. and A. Fokas, *Complex Variables: Introduction and Applications*, 2nd Edition, Cambridge University Press, 2003.
30. Gurler, N. and Y. Z. Ider, "Numerical methods and software tools for simulation, design, and resonant mode analysis of radio frequency birdcage coils used in MRI," *Concepts Magn. Reson. Part B*, Vol. 45B, No. 1, 13–32, 2015.
31. Insko, E. K. and L. Bolinger, "Mapping of the radiofrequency field," *J. Magn. Reson.*, Vol. 103, No. 1, 82–85, 1993.
32. Van Lier, A. L., J. M. Hoogduin, D. L. Polders, V. O. Boer, J. Hendrikse, P. A. Robe, P. A. Woerdeman, J. J. Lagendijk, P. R. Luijten, and C. A. van den Berg, "Electrical conductivity imaging of brain tumours," *Proc. ISMRM 19th Annual Meeting*, 4464, Montréal, QC, Canada, 2011.
33. Vico, F., L. Greengard, and M. Ferrando, "Fast convolution with free-space Green's functions," *J. Comput. Phys.*, Vol. 323, 191–203, 2016.